

# A Simple and Versatile Approach for the Low-Temperature Synthesis of Transition Metal Phosphide Nanoparticles from Metal Chloride Complexes and $\text{P}(\text{SiMe}_3)_3$

Alexandre Sodreau, Hooman Ghazi Zahedi, Rıza Dervişoğlu, Liqun Kang, Julia Menten, Johannes Zenner, Nicole Terefenko, Serena DeBeer, Thomas Wiegand, Alexis Bordet,\* and Walter Leitner\*

Metal chloride complexes react with tris(trimethylsilyl)phosphine under mild condition to produce metal phosphide (TMP) nanoparticles (NPs), and chlorotrimethylsilane as a byproduct. The formation of Si–Cl bonds that are stronger than the starting M–Cl bonds acts as a driving force for the reaction. The potential of this strategy is illustrated through the preparation of ruthenium phosphide NPs using  $[\text{RuCl}_2(\text{cymene})]$  and tris(trimethylsilyl)phosphine at 35 °C. Characterization with a combination of techniques including electron microscopy (EM), X-ray absorption spectroscopy (XAS), and solid-state nuclear magnetic resonance (NMR) spectroscopy, evidences the formation of small (diameter of 1.3 nm) and amorphous NPs with an overall  $\text{Ru}_{50}\text{P}_{50}$  composition. Interestingly, these NPs can be easily immobilized on functional support materials, which is of great interest for potential applications in catalysis and electrocatalysis.  $\text{Mo}_{50}\text{P}_{50}$  and  $\text{Co}_{50}\text{P}_{50}$  NPs can also be synthesized following the same strategy. This approach is simple and versatile and paves the way toward the preparation of a wide range of transition metal phosphide nanoparticles under mild reaction conditions.

properties.<sup>[5]</sup> For example, semiconductors based on TMP (e.g. indium phosphide, cadmium phosphide) are widely used in displays and medical imaging for their luminescent properties. TMP NPs are also of high importance for catalytic<sup>[6]</sup> and electrocatalytic<sup>[7]</sup> applications in the field of chemical energy conversion. For all these applications, NPs size, dispersion, and composition are crucial parameters. However, typical synthetic approaches to the preparation of TMP NPs rely on the use of high temperatures, and/or difficult-to-handle phosphorus sources (see Figure 1a–c for some examples), hindering easy access to well-defined, high-quality TMP NPs.<sup>[1,8]</sup> For example, the use of organic phosphines as precursors (e.g. trioctylphosphine (TOP)) requires temperatures above 250 °C to achieve C–P bond cleavage,<sup>[9]</sup> while the in situ generation of  $\text{PH}_3$  from inorganic phosphates can be achieved at 250 °C.<sup>[10]</sup> The


use of single-source precursors containing both, a transition metal and phosphorus atoms, represents also an alternative but still involves high temperatures (250–350 °C).<sup>[11]</sup> For example, Pinna and co-workers reported a scalable and nonhazardous approach for the controlled synthesis of nanostructured mono and bimetallic TMPs through the pyrolysis of single-source metal–organophosphonates precursors.<sup>[12]</sup> Red phosphorus can be reacted with various transition metals (e.g. Fe, Co, Ni, etc.) at 700–1000 °C to produce the corresponding metal phosphides.<sup>[13]</sup> Such high temperatures tend to give relatively large, polydisperse, agglomerated, or even sintered NPs. Elemental phosphorus  $\text{P}_4$  can also be used for the solvothermal synthesis of  $\text{CoP}_3$ ,  $\text{NiP}_2$ ,  $\text{CuP}_2$ , and  $\text{InP}$  at 150–275 °C.<sup>[14]</sup> Recently, pre-formed metal NPs have been converted to TMP NPs by reaction with  $\text{P}_4$  in solution at 150 °C.<sup>[15]</sup> However,  $\text{P}_4$  is pyrophoric, and its use is a clear safety concern, both in the laboratory and particularly in industrial applications at a larger scale.

Interestingly, high-quality  $\text{InP}$  and  $\text{Cd}_3\text{P}_2$  NPs were shown to be accessible using tris(trimethylsilyl)phosphine ( $\text{P}(\text{SiMe}_3)_3$ ) as phosphorus source,<sup>[17]</sup> taking advantage of the lower stability of P–Si bonds, as compared to P–C bonds (bond dissociation

## 1. Introduction

TMP NPs<sup>[1]</sup> are attracting tremendous attention owing to their excellent optical,<sup>[2]</sup> magnetic,<sup>[3]</sup> electronic,<sup>[4]</sup> and catalytic

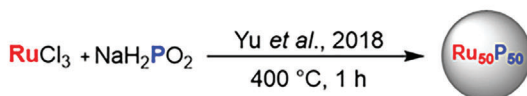
A. Sodreau, H. G. Zahedi, L. Kang, J. Menten, J. Zenner, S. DeBeer, T. Wiegand, A. Bordet, W. Leitner  
Department of Molecular Catalysis  
Max Planck Institute for Chemical Energy Conversion  
45470 Mülheim an der Ruhr, Germany  
E-mail: alexis.bordet@cec.mpg.de; walter.leitner@cec.mpg.de  
H. G. Zahedi, R. Dervişoğlu, J. Zenner, N. Terefenko, T. Wiegand, W. Leitner  
Institute of Technical and Macromolecular Chemistry  
RWTH Aachen University  
Worringerweg 2, 52074 Aachen, Germany

 The ORCID identification number(s) for the author(s) of this article can be found under <https://doi.org/10.1002/adma.202306621>

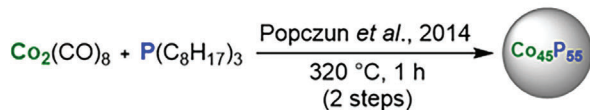
© 2023 The Authors. Advanced Materials published by Wiley-VCH GmbH. This is an open access article under the terms of the Creative Commons Attribution License, which permits use, distribution and reproduction in any medium, provided the original work is properly cited.

DOI: 10.1002/adma.202306621

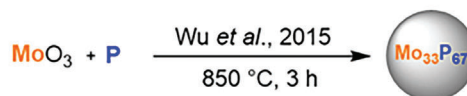
a) High temperature synthesis involving phosphates



b) High temperature synthesis involving TOP



c) High temperature synthesis involving red phosphorous



d) This study:

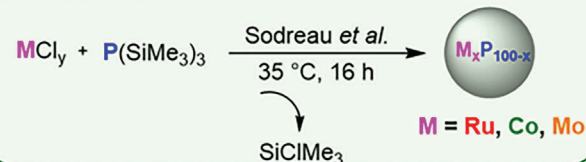


**Figure 1.** a-c) Common high-temperature approaches for the synthesis of TMPs involving transition metal precursors and different phosphorous sources;<sup>[16]</sup> d) Low-temperature synthesis described in this study involving metal chlorides and  $\text{P}(\text{SiMe}_3)_3$ .

energies of  $\approx 331\text{ kJ mol}^{-1}$  and  $\approx 509\text{ kJ mol}^{-1}$ , respectively). This approach was likely inspired by a pioneering work by Barron et al. in which bulk indium phosphide was obtained by reacting  $\text{InCl}_3$  with  $\text{P}(\text{SiMe}_3)_3$  and performing a heat treatment at  $650^\circ\text{C}$ .<sup>[18]</sup> While initial studies on NPs formation reported high temperatures ( $230\text{--}300\text{ }^\circ\text{C}$ ),<sup>[2b]</sup> several groups showed that the reaction could also occur under milder conditions ( $30\text{--}90\text{ }^\circ\text{C}$ ).<sup>[19]</sup> In these cases, carboxylate metal complexes were used, and the insertion of  $\text{P}(\text{SiMe}_3)_3$  into the metal-carboxylate bond was suggested as a potential mechanism for the formation of metal phosphide NPs and trimethylsilyl carboxylates as byproducts. However, only few examples reporting on low-temperature synthesis exist until now, and mainly focus on the formation of quantum dots.<sup>[19]</sup> Thus, the development of simple and versatile synthetic procedures for the preparation of a wide range of size-controlled TMP NPs under mild conditions is highly desired, but remains a challenge.

In this context, we report an alternative route to TMP NPs using simple commercial metal chloride complexes and  $\text{P}(\text{SiMe}_3)_3$  as metal and phosphorus sources, respectively (Figure 1d). This strategy is inspired by early days observations on the formation of In-P and Ga-As bonds,<sup>[18,20]</sup> and relies on the superior strength of the Si-Cl bond (bond dissociation energy  $\approx 490\text{ kJ mol}^{-1}$ ) as compared to most of transition metal-Cl bonds.<sup>[21]</sup> We hypothesize that this difference in bond strengths can act as a driving force for the formation of a variety of metal phosphide NPs, with trimethylsilyl chloride ( $\text{SiClMe}_3$ ) being released as a by-product. Herein, the potential of this strategy is explored first using the synthesis of ruthenium phosphide NPs as a model reaction, and then extended to other metals including cobalt and molybdenum. The preparation of NPs in solution (i.e., isolated) and immobilized on catalytic support materials is investigated. The morphological, structural, and electronic properties of the resulting materials are characterized using a variety of techniques including NMR (solution, and solid state), EM, X-ray diffraction (XRD), and XAS.

## 2. Results and Discussion

### 2.1. Synthesis and Characterization of TMP NPs in solution

Colloidal metal phosphide NPs were prepared by reacting metal chloride complexes with  $\text{P}(\text{SiMe}_3)_3$  in solution. Taking the spe-

cific example of ruthenium phosphide NPs to illustrate the general strategy,  $\text{P}(\text{SiMe}_3)_3$  (0.25 mmol) was added to a mixture of  $[\text{RuCl}_2(\text{cymene})]$  (0.25 mmol, Ru:P ratio 1:1) in dichloromethane  $\text{CH}_2\text{Cl}_2$  (3.6 mL) and magnetically stirred under Ar at  $35\text{ }^\circ\text{C}$  (Figure 2).  $[\text{RuCl}_2(\text{cymene})]$  was selected for its Cl ligands and good solubility in organic solvents. Hexadecylamine (HDA, 0.125–0.25 mmol, 0.5–1.0 equivalent) can be used as ligand to control NPs growth and stability in solution.<sup>[19a]</sup> Upon stirring the resulting mixture under an Ar atmosphere overnight (16 h), the mixture transformed from orange to a dark black stable colloidal solution, suggesting the formation of NPs (Figure S1, Supporting Information). The NPs were precipitated and washed seven times with toluene (5 mL), giving a black powder that was dried under vacuum for 3 h. Other solvents can be used besides  $\text{CH}_2\text{Cl}_2$  (e.g., tetrahydrofuran (THF), mesitylene).

To investigate the reaction kinetics, the distribution of species was monitored over time by  $^1\text{H}$ , and  $^{31}\text{P}$  NMR spectroscopy (Figure 3 and Figure S2–S11, Supporting Information). For this purpose,  $\text{CD}_2\text{Cl}_2$  was used as solvent with mesitylene as internal standard, and the reaction temperature was fixed to  $35\text{ }^\circ\text{C}$ . In the absence of HDA and with a 1:1 stoichiometry between  $[\text{RuCl}_2(\text{cymene})]$  and  $\text{P}(\text{SiMe}_3)_3$ ,  $^1\text{H}$  NMR spectra showed clearly the progressive release of the cymene ligand from  $[\text{RuCl}_2(\text{cymene})]$  ( $^1\text{H}$  chemical-shift change from 5.29 ppm (d) and 5.42 ppm (d) to 7.06–7.14 (m) ppm, Figure 3a), along with the consumption of  $\text{P}(\text{SiMe}_3)_3$  (0.30 ppm) and formation of  $\text{SiClMe}_3$  (0.44 ppm, Figure 3a, spectra in Figure S2–S10, Supporting Information). Traces of  $\text{P}(\text{SiMe}_3)_3$  are still visible even after long reaction times, consistent with the excess of  $\text{SiMe}_3$  in  $\text{P}(\text{SiMe}_3)_3$  with respect to the 2 chlorido ligands of  $[\text{RuCl}_2(\text{cymene})]$  in this 1:1 stoichiometry. This is also clearly visible by plotting the concentrations of the different species as a function of time (Figure 3b). Interestingly, the final concentration of free cymene is reached after  $\approx 13\text{ h}$ , and is as expected from the stoichiometry of the reaction, indicating the complete consumption of the Ru precursor. In contrast, the concentration of  $\text{P}(\text{SiMe}_3)_3$  continues to drop even after this point, resulting in an increase of the  $\text{SiClMe}_3$  concentration above the values expected from the stoichiometry, presumably due to a reaction of excess  $\text{P}(\text{SiMe}_3)_3$  with the solvent  $\text{CD}_2\text{Cl}_2$  to form  $\text{SiClMe}_3$ . This is supported by performing a reaction with a 3:2 stoichiometry between  $[\text{RuCl}_2(\text{cymene})]$  and  $\text{P}(\text{SiMe}_3)_3$ , corresponding to a 1:1 stoichiometry between chlorido ligands and

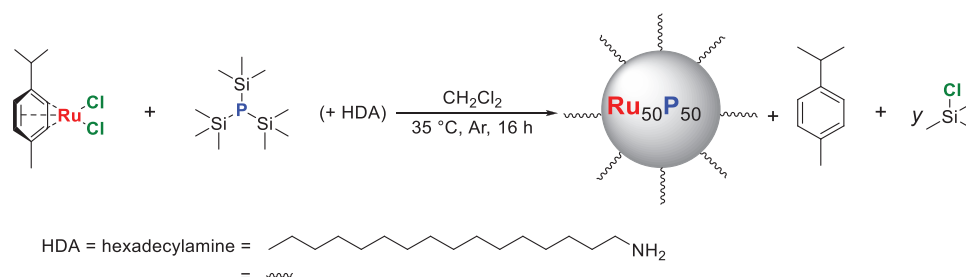


**Figure 2.** Our synthetic approach to metal phosphide NPs illustrated for the preparation of ruthenium phosphide NPs starting from a 1:1 stoichiometry between  $[\text{RuCl}_2(\text{cymene})]$  and  $\text{P}(\text{SiMe}_3)_3$ , giving a theoretical  $\text{Ru}_{50}\text{P}_{50}$  composition.

$\text{SiMe}_3$  (Figure 3c). In this case,  $\text{P}(\text{SiMe}_3)_3$  is fully consumed, and cymene and  $\text{SiClMe}_3$  concentrations reach a plateau at the same reaction time (ca. 10 h), at values exactly as expected from the reaction stoichiometry.

In addition, the course of the reaction was followed in the presence of HDA as a ligand and otherwise standard reaction conditions. NMR monitoring revealed that the  $\text{P}(\text{SiMe}_3)_3$  consumption rate depends strongly on the presence and concentration of the HDA ligand, with slower rates observed when increasing the

amount of HDA (Figure S12, Supporting Information). Without ligand,  $^{31}\text{P}$  NMR monitoring showed the progressive consumption of  $\text{P}(\text{SiMe}_3)_3$  ( $^{31}\text{P}$  resonance at  $-251.0$  ppm) without noticeable formation of intermediates (Figure S11, Supporting Information). In contrast, in the presence of HDA (0.5 – 1 equivalent, Figure S13 and S14, Supporting Information),  $\text{P}(\text{SiMe}_3)_3$  was consumed as well, but an intermediate species progressively appeared at  $-67.2$  ppm. This signal can be tentatively attributed to aminophosphine species. Interestingly, in this case,  $\text{P}(\text{SiMe}_3)_3$

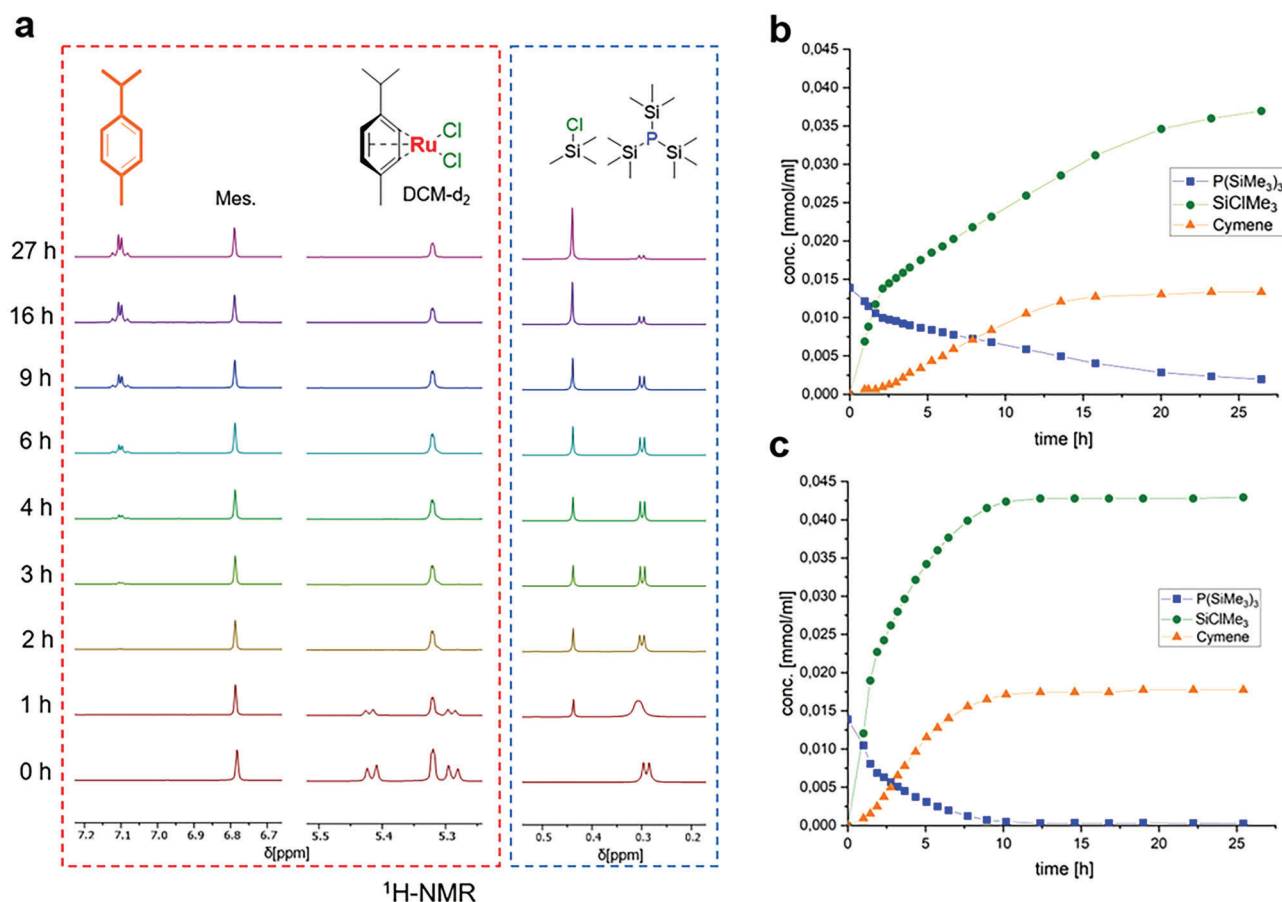


**Figure 3.** Solution-state NMR monitoring of the reaction between  $[\text{RuCl}_2(\text{cymene})]$  and  $\text{P}(\text{SiMe}_3)_3$  at  $35^\circ\text{C}$ , 1:1 stoichiometry, no HDA. a)  $^1\text{H}$  NMR; b) evolutions of the concentrations of  $\text{P}(\text{SiMe}_3)_3$ , cymene ligand, and  $\text{SiClMe}_3$  along the course of the reaction (derived from  $^1\text{H}$  NMR spectra); c) evolutions of the concentrations of  $\text{P}(\text{SiMe}_3)_3$ , cymene ligand, and  $\text{SiClMe}_3$  along the course of a reaction with a 3:2 stoichiometry between  $[\text{RuCl}_2(\text{cymene})]$  and  $\text{P}(\text{SiMe}_3)_3$  (derived from  $^1\text{H}$  NMR spectra). For  $t = 0$  h, the theoretical initial concentration of  $\text{P}(\text{SiMe}_3)_3$  and the  $^1\text{H}$  NMR spectrum of pure  $\text{P}(\text{SiMe}_3)_3$  were used. Mes = mesitylene was used as internal standard.



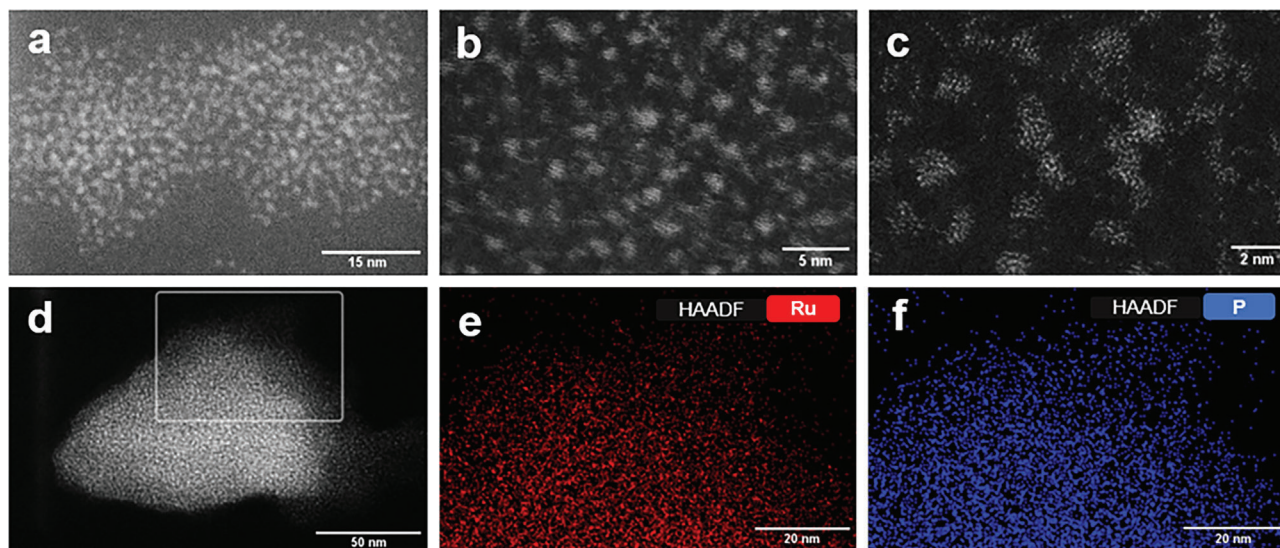


**Figure 4.** a–d) STEM-HAADF images at different magnifications of  $\text{Ru}_{50}\text{P}_{50}$  NPs stabilized by 0.5 eq. HDA; e) STEM-HAADF-EDX elemental mapping of Ru-L $\alpha$ ; f) STEM-HAADF-EDX elemental mapping of P-K $\alpha$ .

is fully consumed after 6 h, and only traces of the intermediate are visible at the end of the reaction.

The formation of Ru phosphide NPs under mild conditions can be rationalized based on thermodynamic considerations, as the bond dissociation energy of Si–Cl ( $490.1 \text{ kJ mol}^{-1}$ ) is substantially higher than that of Ru–Cl ( $337.6 \text{ kJ mol}^{-1}$ ) and P–Si ( $363.6 \text{ kJ mol}^{-1}$ ).<sup>[21]</sup> Thus, the formation of Si–Cl bonds (in  $\text{SiClMe}_3$ ) acts as a driving force to break Ru–Cl (in  $[\text{RuCl}_2(\text{cymene})]$ ) and P–Si (in  $\text{P}(\text{SiMe}_3)_3$ ) bonds and leads to the formation  $\text{Ru}_x\text{P}_{100-x}$  materials. Characterization of ruthenium phosphide NPs prepared under standard conditions (0.5 eq. HDA, in  $\text{CH}_2\text{Cl}_2$ ) by inductively coupled plasma optical emission spectroscopy (ICP-OES, Table S1, Supporting Information) showed a Ru:P ratio (42:58) in fair agreement with the starting stoichiometry and theoretical composition (50:50). In the following, these ruthenium phosphide NPs will be referred to as  $\text{Ru}_{50}\text{P}_{50}$  NPs, reflecting the global composition of the material. Analysis by scanning transmission electron microscopy in high-angle annular dark field (STEM-HAADF) revealed the formation of small and well-dispersed NPs ( $d = 1.3 \pm 0.2 \text{ nm}$ , Figure 4a–c and Figure S15) containing both Ru and P, as evidenced by elemental mapping using STEM-HAADF with energy dispersive X-ray spectroscopy (STEM-HAADF-EDX, Figure 4e–f, Figure S16, Supporting Information). Increasing the amount of HDA to 1 equivalent did not affect the NPs composition or size (Table S1, Figure S17, Supporting Information). Performing the reaction in THF instead of  $\text{CH}_2\text{Cl}_2$  resulted in larger NPs ( $3.0 \text{ nm} \pm 0.8 \text{ nm}$ , Figure S18a, Supporting Information), still with Ru and P well-dispersed throughout the particles as showed by STEM-HAADF-EDX (Figure S18b–g, Supporting Information).

However, the structure of  $\text{Ru}_{50}\text{P}_{50}$  NPs remains challenging to resolve due to their amorphous nature and small size. Additionally, the presence of organic ligands covering the NPs surfaces makes it difficult to characterize the oxidation states of Ru species using X-ray photoelectron spectroscopy (XPS). Therefore, XAS characterization was performed to investigate the electronic

and geometric structure of the Ru species within the  $\text{Ru}_{50}\text{P}_{50}$  NPs (Figure 5, and see SI for additional information). By utilizing hard X-rays at the Ru K-edge, which can penetrate the entire particles, the average information regarding all Ru species in the bulk could be obtained. This information included the electronic structure revealed by X-ray absorption near edge structure (XANES) and the geometric structure revealed by extended X-ray absorption fine structure (EXAFS). Figure 5a shows the Ru K-edge XANES spectra of  $\text{Ru}_{50}\text{P}_{50}$  NPs and Ru references.

The absorption edge position in XANES spectra of the  $\text{Ru}_{50}\text{P}_{50}$  NPs is slightly shifted in towards higher energies compared to Ru foil, resembling the absorption edge of  $[\text{Ru}(\text{PPh}_3)_3\text{Cl}_2]$  which suggests the presence of Ru–P bonding in the  $\text{Ru}_{50}\text{P}_{50}$  NPs. To further investigate the structural details, the EXAFS spectrum of  $\text{Ru}_{50}\text{P}_{50}$  NPs (Figure 5b) was fitted. The EXAFS fitting results exhibit a Ru–P coordination at  $2.32 \pm 0.01 \text{ \AA}$  and Ru–Ru coordination at  $2.84 \pm 0.01 \text{ \AA}$ . The coordination numbers (C.N.) were found to be  $4.6 \pm 0.5$  for Ru–P and  $3.5 \pm 0.8$  for Ru–Ru (Table S2, Supporting Information). Interestingly, these results do not align well with those observed in the reference ruthenium phosphide compounds (listed in Table S3, Supporting Information, including  $\text{RuP}_2$ ,  $\text{RuP}$ , and  $\text{Ru}_2\text{P}$ ), suggesting a specific average local atomic arrangement around the Ru sites within the Ru NPs. For instance, the Ru–P coordination number (C.N.) in  $\text{Ru}_{50}\text{P}_{50}$  NPs ( $4.6 \pm 0.5$ ) is significantly smaller than that in  $\text{RuP}$  and  $\text{RuP}_2$  (C.N. = 6), while the Ru–Ru coordination number in  $\text{Ru}_{50}\text{P}_{50}$  NPs ( $3.5 \pm 0.8$ ) is larger than that in  $\text{RuP}_2$  (C.N. = 2) but considerably smaller than in  $\text{RuP}$  and  $\text{Ru}_2\text{P}$ .

In the EXAFS fitting models, the Debye–Waller factor (DWF) is another important parameter for the distribution/variation of interatomic distance of a specific scattering path. In this case, since the XAS spectrum was collected at 15 K, a temperature at which the thermal motion has negligible contribution to the bond length variations, the DWF could be used to estimate the degree of disorder of the coordination structure. Notably, the DWF values for both Ru–P and Ru–Ru scattering paths ( $0.007 \pm 0.001$  and

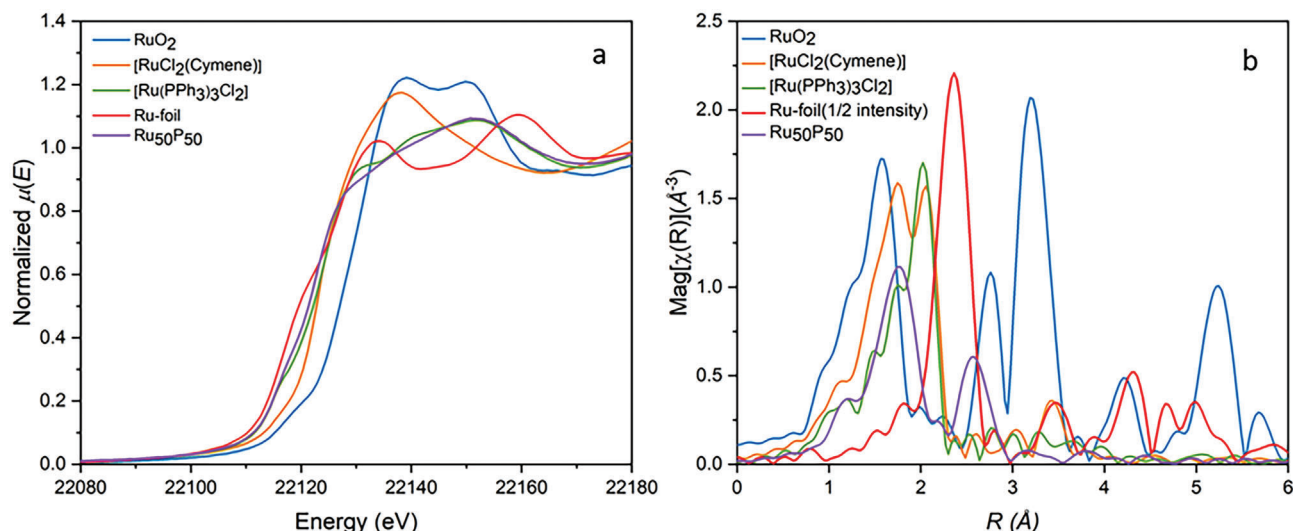


**Figure 5.** Ru K-edge XAS of Ru-foil, RuO<sub>2</sub>, [RuCl<sub>2</sub>(Cymene)], [Ru(PPh<sub>3</sub>)<sub>3</sub>Cl<sub>2</sub>], and Ru<sub>50</sub>P<sub>50</sub> NPs. a) Normalized XANES spectra and b) k<sub>2</sub>-weighted R-space Fourier transformed EXAFS. The R-space Fourier transformed EXAFS spectra are plotted without phase correction.

0.008 ± 0.002, respectively) are relatively large compared to the DWF values of other scattering paths in the reference samples (≈0.003), suggesting the presence of disordered coordination environments around Ru sites and the poor crystallinity nature of the Ru<sub>50</sub>P<sub>50</sub> NP structure. In addition, considering that the ratio between the C.N. of Ru–P and Ru–Ru paths is not in line with any of the commonly known ruthenium phosphides (Table S3, Supporting Information), the actual composition of Ru<sub>50</sub>P<sub>50</sub> NPs likely consists of a mixture of multiple ruthenium phosphide phases, which is also supported by the solid-state NMR data (*vide infra*). In future studies, NPs crystallinity may be controlled by adjusting the reaction parameters (e.g., synthesis temperature, nature and quantity of ligands, etc.), while tuning the Cl content in ruthenium precursors can potentially provide access to NPs with different Ru:P ratios.

We next turned to solid-state NMR to characterize the local environments of <sup>31</sup>P nuclei within the formed Ru<sub>50</sub>P<sub>50</sub> NPs. Based on the metallic character of such NPs, a large <sup>31</sup>P chemical-shift dispersion is expected that is caused by the interaction of conduction electrons with the nuclei, denoted as Knight shifts,<sup>[22]</sup> see also ref.[23] for a recent review. We thus recorded static <sup>31</sup>P spectra using the Wideband Uniform Smooth Truncation-Carr-Purcell Meiboom-Gill (WURSTCPMG) scheme<sup>[24]</sup> to en-

sure uniform excitation of the entire spectrum. **Figure 6a** shows the <sup>31</sup>P WURST-CPMG spectrum of Ru<sub>50</sub>P<sub>50</sub> NPs. The envelope of the observed “spikelet pattern” forms the static <sup>31</sup>P NMR line shape. Line-shape simulation<sup>[25]</sup> following the procedure described in ref.[26] has been achieved using four ambiguous Gaussian/Lorentzian peaks, which indicate different phosphorus species within the NPs (see Figure 6a and Table S4, Supporting Information), as already indicated by the XAS measurements (see above). The broad static <sup>31</sup>P NMR line shape might be dominated by <sup>31</sup>P Knight-shift distributions due to structural and surface electronic effects in the NPs, as reported recently for NiP<sub>2</sub> NPs.<sup>[27]</sup> The species at high ppm-values (415 and 622 ppm) can be assigned to Ru<sub>x</sub>P<sub>100-x</sub> phases in which the phosphorus nuclei experience a positive Knight shift (as observed in other transition metal phosphides as well),<sup>[13,27,28]</sup> whereas the <sup>31</sup>P resonances at lower ppm-values (49 and 187 ppm) belong to further, probably diamagnetic, phosphorus-containing species. Similar resonances have been observed previously in a study in which Ru<sub>x</sub>P<sub>100-x</sub> NPs were synthesized using white phosphorus as P-source and assigned to species with lower local Ru content around the phosphorus nuclei (155 ppm) and oxidized species (–21 ppm).<sup>[29]</sup> The <sup>31</sup>P WURST-CPMG spectrum of the Ru<sub>x</sub>P<sub>100-x</sub> NPs reported previously<sup>[29]</sup> is quite similar to the one reported

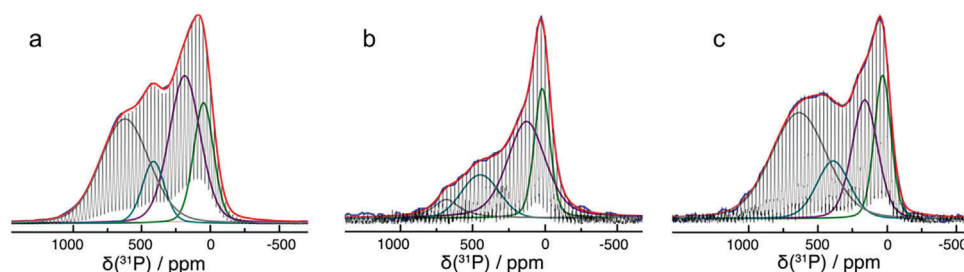


**Figure 6.** Static <sup>31</sup>P WURST-CPMG spectra of Ru<sub>50</sub>P<sub>50</sub> a), Mo<sub>50</sub>P<sub>50</sub> b) and Ru<sub>50</sub>P<sub>50</sub>@SILP c) measured at 11.7 T. Peak deconvolutions with four components using Gaussian/Lorentzian peaks are shown as colored lines and their sum as a red line. The blue line is the envelope of the spikelet pattern. See Table S4, Supporting Information for details.



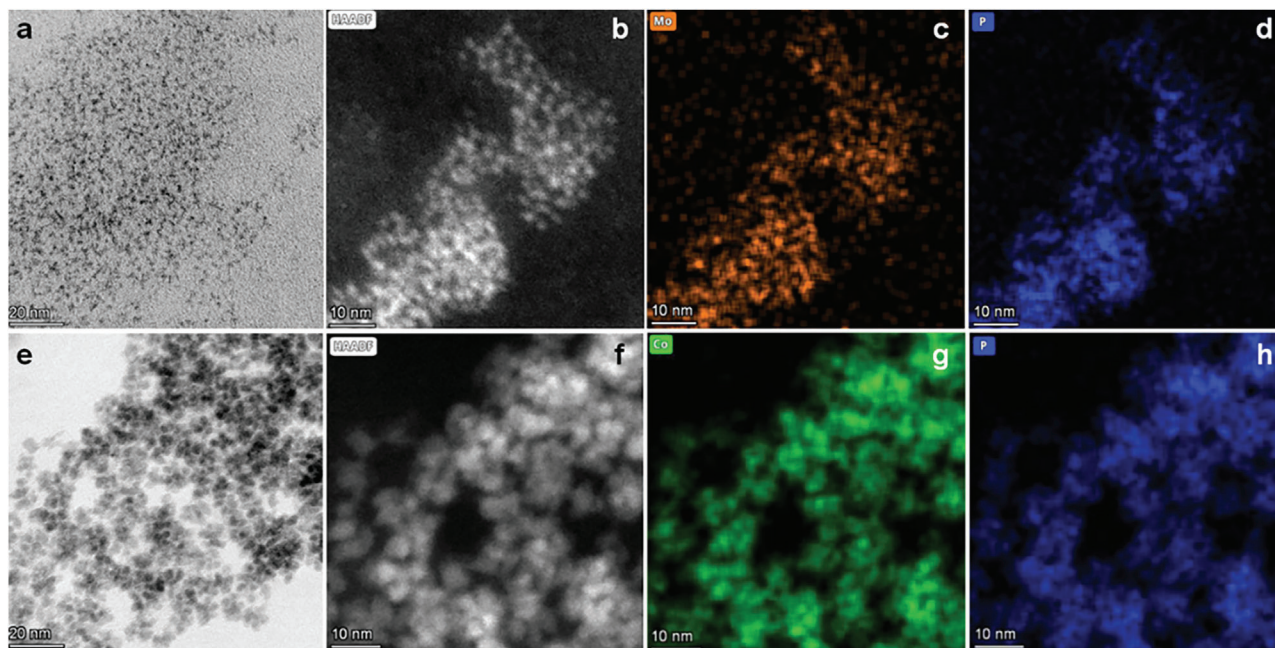


**Figure 7.** a) TEM image of  $\text{Mo}_{50}\text{P}_{50}$  NPs; b) STEM-HAADF image of  $\text{Mo}_{50}\text{P}_{50}$  NPs; c) STEM-HAADF-EDX elemental mapping of Mo-L $\alpha$ ; d) STEM-HAADF-EDX elemental mapping of P-K $\alpha$ ; e) TEM picture of  $\text{Co}_{50}\text{P}_{50}$  NPs; f) STEM-HAADF image of  $\text{Co}_{50}\text{P}_{50}$  NPs; g) STEM-HAADF-EDX elemental mapping of Co-K $\alpha$ ; h) STEM-HAADF-EDX elemental mapping of P-K $\alpha$ .

here (Figure 6a), also featuring the high-ppm species assigned to  $\text{Ru}_x\text{P}_{100-x}$  NPs. To probe the effect of oxidation on the samples, a part of the sample was exposed to air for 28 days. The  $^{31}\text{P}$  WURST-CPMG spectrum (Figure S19, Supporting Information) of the exposed sample is dominated by the low-ppm species, indeed suggesting sample oxidation.

Satisfyingly, small and well-dispersed cobalt phosphide NPs ( $d = 3.4 \pm 0.5$  nm) and molybdenum phosphide NPs ( $d = 1.3 \pm 0.2$  nm) could also be successfully synthesized in THF following the same strategy using cobalt(II)-chloride [ $\text{CoCl}_2$ ] and trichlorotris(tetrahydrofuran)molybdenum(III) [ $\text{Mo}(\text{THF})_3\text{Cl}_3$ ] as precursors and 0.5 equivalent of HDA, highlighting the versatility of our synthetic approach (Figure 7a–h and Figure S20, Supporting Information). For these materials, elemental analysis by ICP-OES determined M:P ratios in excellent agreement with the starting stoichiometry (50:50, Table S1, Supporting Information). We recorded  $^{31}\text{P}$  WURST-CPMG spectra on the  $\text{Mo}_{50}\text{P}_{50}$  NPs (Figure 6b), also revealing the successful formation of metal phosphide NPs as concluded from high-ppm  $^{31}\text{P}$  resonances effected by sizeable Knight-shift distributions.

## 2.2. Synthesis and Characterization of Supported TMP NPs

For catalytic and electrocatalytic applications, the immobilization of TMP NPs on support materials represents an important step in the development of stable and easy-to-handle catalysts.<sup>[7f]</sup> In this context, we investigated the possibility to immobilize  $\text{Ru}_{50}\text{P}_{50}$  NPs on an imidazolium-based supported ionic liquid phase (SILP). This SILP has been widely used for the preparation and stabilization of monometallic and bimetallic NPs used as hydrogenation, hydrodeoxygenation, and hydrogenolysis

catalysts.<sup>[30]</sup> The wet impregnation of the SILP with  $\text{Ru}_{50}\text{P}_{50}$  NPs prepared as described above proved straightforward and successful (Figure S21, and protocol available in the SI). In addition, we explored the possibility to synthesize  $\text{Ru}_{50}\text{P}_{50}$  NPs directly in the presence of the SILP, in an in situ approach. For that, the SILP (500 mg) was added to a solution of  $\text{P}(\text{SiMe}_3)_3$  (0.25 mmol) and  $[\text{RuCl}_2(\text{cymene})]$  (0.25 mmol) in  $\text{CH}_2\text{Cl}_2$  (Figure 8a). The resulting mixture was stirred at 35 °C for 16 h, giving a black powder that was washed 6 times with toluene and dried in vacuo. Characterization of the resulting material by STEM-HAADF evidenced the formation of small ( $d = 1.6$  nm  $\pm$  0.2 nm) and well-dispersed NPs on the SILP (Figure 8 and Figure S22, Supporting Information). STEM-HAADF-EDX line scans confirmed that the formed NPs contain both Ru and P. ICP-OES analysis determined a Ru loading of 3.87 wt.%, with a Ru:P molar ratio of 51:49 determined by scanning electron microscopy (SEM)-EDX. This ratio is consistent with the theoretical value based on the reaction stoichiometry. Interestingly, only traces of Cl can be detected by elemental analysis (Table S5, Supporting Information), indicating that the formation of  $\text{SiClMe}_3$  effectively “traps” the Cl released from the  $[\text{RuCl}_2(\text{cymene})]$  precursor also under these conditions.

In addition,  $\text{Ru}_{50}\text{P}_{50}$ @SILP materials prepared by ex situ and in situ approaches were characterized by XAS (Figure 9, see SI for additional information).

Comparing the XANES spectrum of  $\text{Ru}_{50}\text{P}_{50}$ @SILP samples to that of  $\text{Ru}_{50}\text{P}_{50}$  NPs, it is evident that they exhibit nearly identical absorption edge peak shape and position (Figure 9a). Such similarity suggests that the electronic structure of the Ru species in  $\text{Ru}_{50}\text{P}_{50}$ @SILP, whether prepared ex situ or in situ, is nearly identical to that of  $\text{Ru}_{50}\text{P}_{50}$  NPs. Furthermore, the EXAFS fitting results (Figure 9b) for Ru-SILP support its structural resemblance to RuP NPs, featuring Ru-P and Ru-Ru coordination at

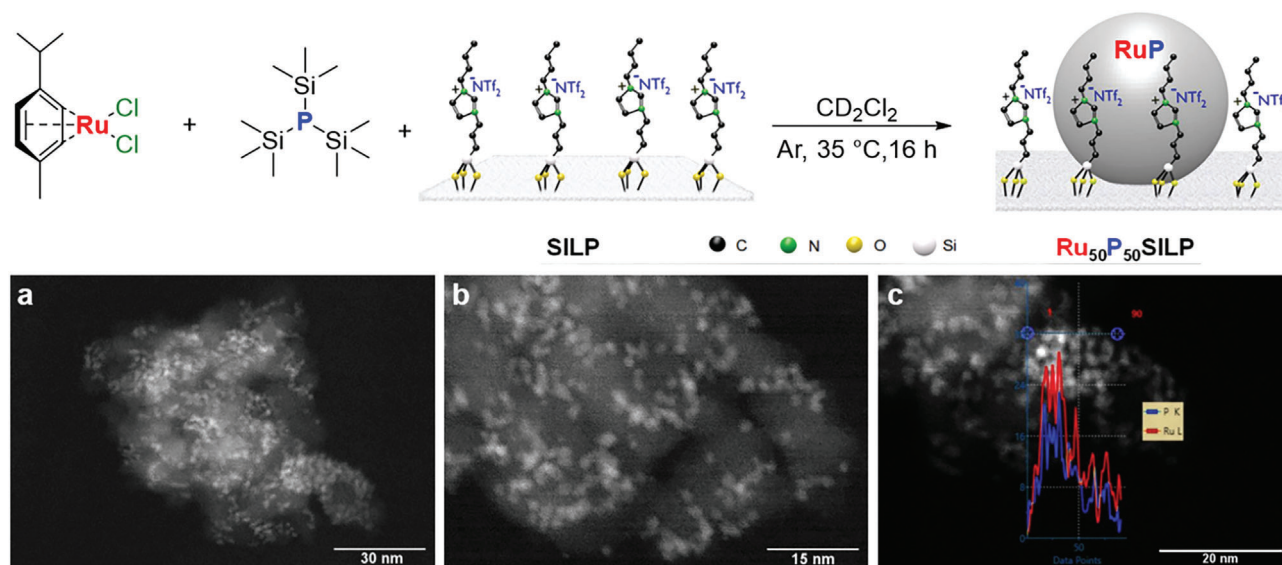


**Figure 8.** a) Synthesis of  $\text{Ru}_{50}\text{P}_{50}@SILP$  via an in-situ approach; b) and c) STEM-HAADF pictures; d) STEM-HAADF-EDX line scans of several NPs showing the presence of Ru and P.

distances of  $2.31 \pm 0.01 \text{ \AA}$  and  $2.82 \pm 0.01 \text{ \AA}$ , respectively. The only discernible difference lies in the second coordination shell, where  $\text{Ru}_{50}\text{P}_{50}@SILP$  exhibits a slightly larger coordination number for Ru-Ru ( $4.5 \pm 0.5$ ) compared to  $\text{Ru}_{50}\text{P}_{50}$  NPs ( $3.5 \pm 0.8$ ), which is consistent with the slightly increased particle size observed in  $\text{Ru}_{50}\text{P}_{50}@SILP$  (1.6 nm) compared to isolated  $\text{Ru}_{50}\text{P}_{50}$  NPs (1.3 nm). However, due to the complex synthesis mechanism involved in producing  $\text{Ru}_{50}\text{P}_{50}$  NPs with or without SILP support, further investigations are necessary to gain a better understanding of the role of SILP support in processes such as nucleation, particle growth, particle recrystallization, and potentially even Ostwald ripening within this system.

The  $^{31}\text{P}$  WURST-CPMG spectrum recorded on the in situ prepared  $\text{Ru}_{50}\text{P}_{50}@SILP$  material (Figure 6c) resembles the one of

the pure NPs (Figure 6a) with respect to both, the peak positions of the Gaussian/Lorentzian lines used to simulate the spectrum as well as the relative ratios of the resonances (see Table S4, Supporting Information for details).

### 3. Conclusion

In conclusion, we herein report a versatile pathway for the synthesis of TMPs NPs under mild conditions. Taking ruthenium phosphide as a case study,  $\text{P}(\text{SiMe}_3)_3$  was shown to react smoothly with the organometallic precursor  $[\text{RuCl}_2(\text{cymene})]$  to produce ruthenium phosphide NPs at  $35^\circ\text{C}$ , with the formation of  $\text{SiClMe}_3$  as a by-product. Following this approach, small and well-dispersed NPs could be synthesized both isolated in solution, and

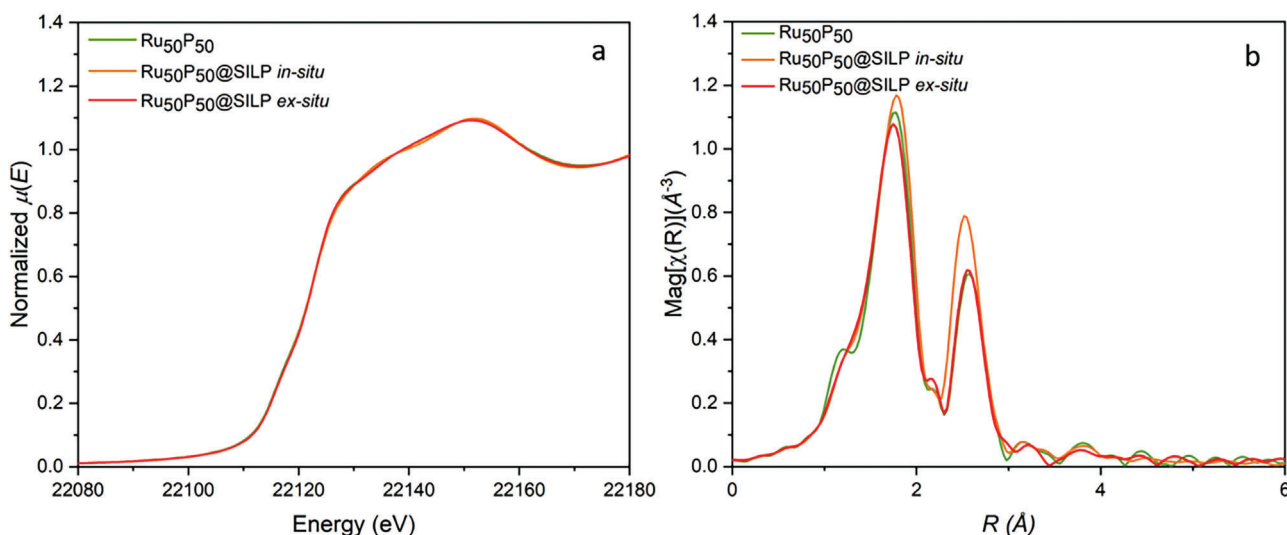


**Figure 9.** Ru K-edge XAS of  $\text{Ru}_{50}\text{P}_{50}@SILP$  materials. (a) Normalized XANES spectra and (b)  $k^2$ -weighted R-space Fourier transformed EXAFS of  $\text{Ru}_{50}\text{P}_{50}$  NPs,  $\text{Ru}_{50}\text{P}_{50}@SILP$  ex situ, and  $\text{Ru}_{50}\text{P}_{50}@SILP$  in situ. The R-space Fourier transformed EXAFS spectra are plotted without phase correction.

immobilized on a functional support. In-depth characterization of these NPs using in particular electron microscopy, XAS, and solid-state NMR evidenced that they consist of a mixture of ruthenium phosphide phases, with a Ru<sub>50</sub>P<sub>50</sub> global composition. The versatility and simplicity of this synthetic approach was demonstrated through the preparation of cobalt phosphide and molybdenum phosphide NPs. The exploitation of the strength of the Si-Cl bond as compared to many metal-Cl bonds is expected to provide easy access to a wide range of transition metal phosphide nanoparticles.

## Supporting Information

Supporting Information is available from the Wiley Online Library or from the author.

## Acknowledgements

A.S. and H.G.Z. contributed equally to this work. The authors appreciate the funding by the Max Planck Society and by the Deutsche Forschungsgemeinschaft (DFG, German Research Foundation) under Germany's Excellence Strategy – Exzellenzcluster 2186 “The Fuel Science Center” ID: 390919832. T.W. acknowledges support from the Deutsche Forschungsgemeinschaft (Heisenberg fellowship, project number 455238107). T.W. thanks Dr. René Verel (ETH Zürich, Switzerland) for sharing the WURST-CPMG pulse sequence. L.K. acknowledges Alexander von Humboldt Foundation for a postdoctoral fellowship and funding support. The authors acknowledge DESY (Hamburg, Germany), a member of the Helmholtz Association HGF, for the provision of experimental facilities. For parts of this research carried out at PETRA III under proposal I-20211319, the authors would like to thank Dr. Edmund Welter for assistance in using beamline P65. The authors acknowledge Diamond Light Source (UK) and electron Physical Science Imaging Centre (ePSIC) for experiment time on E02 under proposal MG33118. The authors would like to thank Dr. David Hopkinson, Dr. Chris Allen and Dr. Mohsen Danaie and for their assistance during the experiment session.

Open access funding enabled and organized by Projekt DEAL.

## Conflict of Interest

The authors declare no conflict of interest.

## Data Availability Statement

The data that support the findings of this study are available in the supplementary material of this article.

## Keywords

metal phosphide, nanoparticles, ruthenium phosphide, synthesis

Received: July 6, 2023

Revised: September 26, 2023

Published online: October 22, 2023

- [1] S. Carenco, D. Portehault, C. Boissière, N. Mézailles, C. Sanchez, *Chem. Rev.* **2013**, *113*, 7981.

- [2] a) B. Chen, D. Li, F. Wang, *Small* **2020**, *16*, 2002454; b) L. Li, P. Reiss, *J. Am. Chem. Soc.* **2008**, *130*, 11588; c) Y.-H. Won, O. Cho, T. Kim, D.-Y. Chung, T. Kim, H. Chung, H. Jang, J. Lee, D. Kim, E. Jang, *Nature* **2019**, *575*, 634; d) S. Miao, S. G. Hickey, B. Rellinghaus, C. Waurisch, A. Eyckmüller, *J. Am. Chem. Soc.* **2010**, *132*, 5613; e) R. Xie, D. Battaglia, X. Peng, *J. Am. Chem. Soc.* **2007**, *129*, 15432.
- [3] a) O. Tegus, E. Brück, K. H. J. Buschow, F. R. De Boer, *Nature* **2002**, *415*, 150; b) S. L. Brock, S. C. Perera, K. L. Stamm, *Chemistry* **2004**, *10*, 3364.
- [4] a) X. Jiang, Q. Xiong, S. Nam, F. Qian, Y. Li, C. M. Lieber, *Nano Lett.* **2007**, *7*, 3214; b) M. R. Khan, K. Bu, J.-S. Chai, J.-T. Wang, *Sci. Rep.* **2020**, *10*, 11502; c) J.-H. Pöhls, A. Faghaninia, G. Petretto, U. Aydemir, F. Ricci, G. Li, M. Wood, S. Ohno, G. Hautier, G. J. Snyder, G.-M. Rignanese, A. Jain, M. A. White, *J. Mater. Chem. C* **2017**, *5*, 12441; d) M. Pramanik, S. Tominaka, Z.-L. Wang, T. Takei, Y. Yamauchi, *Angew. Chem., Int. Ed.* **2017**, *56*, 13508.
- [5] a) A.-M. Alexander, J. S. J. Hargreaves, *Chem. Soc. Rev.* **2010**, *39*, 4388; b) S.-H. Li, M.-Y. Qi, Z.-R. Tang, Y.-J. Xu, *Chem. Soc. Rev.* **2021**, *50*, 7539.
- [6] a) S. T. Oyama, T. Gott, H. Zhao, Y.-K. Lee, *Catal. Today* **2009**, *143*, 94; b) K. Li, R. Wang, J. Chen, *Energy Fuels* **2011**, *25*, 854; c) H. Xin, Y. Liu, C. Hu, J. A. Lercher, *J. Catal.* **2021**, *401*, 129; d) S. Yamaguchi, S. Fujita, K. Nakajima, S. Yamazoe, J. Yamasaki, T. Mizugaki, T. Mitsudome, *Green Chem.* **2021**, *23*, 2010; e) T. Mitsudome, M. Sheng, A. Nakata, J. Yamasaki, T. Mizugaki, K. Jitsukawa, *Chem. Sci.* **2020**, *11*, 6682.
- [7] a) E. J. Popczun, J. R. McKone, C. G. Read, A. J. Baciocchi, A. M. Wiltrout, N. S. Lewis, R. E. Schaak, *J. Am. Chem. Soc.* **2013**, *135*, 9267; b) V. V. T. Doan-Nguyen, S. Zhang, E. B. Trigg, R. Agarwal, J. Li, D. Su, K. I. Winey, C. B. Murray, *ACS Nano* **2015**, *9*, 8108; c) Y. Shi, B. Zhang, *Chem. Soc. Rev.* **2016**, *45*, 1529; d) C. A. Downes, K. M. Van Allsburg, S. A. Tacey, K. A. Unocic, F. G. Baddour, D. A. Ruddy, N. J. Libretto, M. M. O'Connor, C. A. Farberow, J. A. Schaidle, S. E. Habas, *Chem. Mater.* **2022**, *34*, 6255; e) J. Kibsgaard, C. Tsai, K. Chan, J. D. Benck, J. K. Nørskov, F. Abild-Pedersen, T. F. Jaramillo, *Energy Environ. Sci.* **2015**, *8*, 3022; f) A. Parra-Puerto, K. L. Ng, K. Fahy, A. E. Goode, M. P. Ryan, A. Kucernak, *ACS Catal.* **2019**, *9*, 11515.
- [8] S. Carenco, D. Portehault, C. Boissière, N. Mézailles, C. Sanchez, *Adv. Mater.* **2014**, *26*, 371.
- [9] a) A. E. Henkes, R. E. Schaak, *Chem. Mater.* **2007**, *19*, 4234; b) T. Su'a, M. N. Poli, S. L. Brock, *ACS Nanosci Au* **2022**, 503.
- [10] R. Zhou, J. Zhang, Z. Chen, X. Han, C. Zhong, W. Hu, Y. Deng, *Electrochim. Acta* **2017**, *258*, 866.
- [11] S. E. Habas, F. G. Baddour, D. A. Ruddy, C. P. Nash, J. Wang, M. Pan, J. E. Hensley, J. A. Schaidle, *Chem. Mater.* **2015**, *27*, 7580.
- [12] a) R. Zhang, P. A. Russo, M. Feist, P. Amsalem, N. Koch, N. Pinna, *ACS Appl. Mater. Interfaces* **2017**, *9*, 14013; b) S. M. El-Refaei, P. A. Russo, P. Amsalem, N. Koch, N. Pinna, *ACS Appl. Nano Mater.* **2020**, *3*, 4147; c) S. M. El-Refaei, P. A. Russo, T. Schultz, N. Koch, N. Pinna, *ChemCatChem* **2021**, *13*, 4392.
- [13] E. Bekaert, J. Bernardi, S. Boyanov, L. Monconduit, M.-L. Doublet, M. Ménétrier, *J. Phys. Chem. C* **2008**, *112*, 20481.
- [14] a) B. M. Barry, E. G. Gillan, *Chem. Mater.* **2008**, *20*, 2618; b) E. Bang, Y. Choi, J. Cho, Y.-H. Suh, H. W. Ban, J. S. Son, J. Park, *Chem. Mater.* **2017**, *29*, 4236; c) P. Yan, Y. Xie, W. Wang, F. Liu, Y. Qian, *J. Mater. Chem.* **1999**, *9*, 1831.
- [15] A.-M. Nguyen, M. Bahri, S. Dreyfuss, S. Moldovan, A. Miche, C. Méthivier, O. Ersen, N. Mézailles, S. Carenco, *Chem. Mater.* **2019**, *31*, 6124.
- [16] a) J. Yu, Y. Guo, S. She, S. Miao, M. Ni, W. Zhou, M. Liu, Z. Shao, *Adv. Mater.* **2018**, *30*, 1800047; b) E. J. Popczun, C. G. Read, C. W. Roske, N. S. Lewis, R. E. Schaak, *Angew. Chem., Int. Ed.* **2014**, *53*, 5427; c) T. Wu, S. Chen, D. Zhang, J. Hou, *J. Mater. Chem. A* **2015**, *3*, 10360.



- [17] a) M. A. Matchett, A. M. Viano, N. L. Adolphi, R. D. Stoddard, W. E. Buhro, M. S. Conradi, P. C. Gibbons, *Chem. Mater.* **1992**, 4, 508; b) W. E. Buhro, *Polyhedron* **1994**, 13, 1131.
- [18] M. D. Healy, P. E. Laibinis, P. D. Stupik, A. R. Barron, *J. Chem. Soc., Chem. Commun.* **1989**, 6, 359.
- [19] a) P. M. Allen, B. J. Walker, M. G. Bawendi, *Angew. Chem., Int. Ed.* **2010**, 49, 760; b) W.-S. Ojo, S. Xu, F. Delpech, C. Nayral, B. Chaudret, *Angew. Chem., Int. Ed.* **2012**, 51, 738.
- [20] C. G. Pitt, A. P. Purdy, K. T. Higa, R. L. Wells, *Organometallics* **1986**, 5, 1266.
- [21] Y.-R. Luo, *Comprehensive Handbook of Chemical Bond Energies*, CRC Press, Boca Raton, USA **2007**.
- [22] W. D. Knight, *Phys. Rev.* **1949**, 76, 1259.
- [23] A. J. Pell, G. Pintacuda, C. P. Grey, *Prog. Nucl. Magn. Reson. Spectrosc.* **2019**, 111, 1.
- [24] A. W. Macgregor, L. A. O'dell, R. W. Schurko, *J. Magn. Reson.* **2011**, 208, 103.
- [25] D. Massiot, F. Fayon, M. Capron, I. King, S. Le Calvé, B. Alonso, J.-O. Durand, B. Bujoli, Z. Gan, G. Hoatson, *Magn. Reson. Chem.* **2002**, 40, 70.
- [26] A. Mahun, S. Abbrent, J. Czernek, J. Rohlicek, H. Macková, W. Ning, R. Konefał, J. Brus, L. Kobera, *Molecules* **2021**, 26, 60517.
- [27] W. Papawassiliou, J. P. Carvalho, N. Panopoulos, Y. Al Wahedi, V. K. S. Wadi, X. Lu, K. Polychronopoulou, J. B. Lee, S. Lee, C. Y. Kim, H. J. Kim, M. Katsiotis, V. Tzitzios, M. Karagianni, M. Fardis, G. Papavassiliou, A. J. Pell, *Nat. Commun.* **2021**, 12, 4334.
- [28] a) I. Furo, I. Bakonyi, K. Tompa, E. Zsoldos, I. Heinmaa, M. Alla, E. Lippmaa, *J. Phys.: Condens. Matter* **1990**, 2, 4217; b) S. Li, Y. Kobayashi, M. Itoh, D. Hirai, H. Takagi, *Phys. Rev. B* **2017**, 95, 155137; c) C. Stinner, Z. Tang, M. Haouas, T. h. Weber, R. Prins, *J. Catal.* **2002**, 208, 456.
- [29] M. Vanni, G. Provinciali, F. D. Calvo, E. Carignani, S. Dreyfuss, N. Mézailles, A. M. Mio, G. Nicotra, S. Caporali, S. Borsacchi, M. Peruzzini, M. Caporali, *ChemCatChem* **2022**, 14, 202200685.
- [30] A. Bordet, W. Leitner, *Acc. Chem. Res.* **2021**, 54, 2144.